

Parametric decay instabilities of lower hybrid waves on CFETR

Taotao Zhou(周涛涛), Nong Xiang(项农), Chunyun Gan(甘春芸),Guozhang Jia(贾国章), and Jiale Chen(陈佳乐)
Citation: Chin. Phys. B, 2022, 31 (**9**): 095201. DOI: 10.1088/1674-1056/ac67c2
Journal homepage: http://cpb.iphy.ac.cn; http://iopscience.iop.org/cpb

What follows is a list of articles you may be interested in

Plasma-wave interaction in helicon plasmas near the lower hybrid frequency

Yide Zhao(赵以德), Jinwei Bai(白进纬), Yong Cao(曹勇), Siyu Wu(吴思宇), Eduardo Ahedo, Mario Merino, and Bin Tian(田滨)
Chin. Phys. B, 2022, 31 (**7**): 075203. DOI: 10.1088/1674-1056/ac40fd

Reduction of impurity confinement time by combined heating of LHW and ECRH in EAST

Zong Xu(许棕), Zhen-Wei Wu(吴振伟), Ling Zhang(张凌), Yue-Heng Huang(黄跃恒), Wei Gao(高伟), Yun-Xin Cheng(程云鑫), Xiao-Dong Lin(林晓东), Xiang Gao(高翔), Ying-Jie Chen(陈颖杰), Lei Li(黎嫘), Yin-Xian Jie(揭银先), Qing Zang(臧庆), Hai-Qing Liu(刘海庆), and EAST team
Chin. Phys. B, 2021, 30 (**7**): 075205. DOI: 10.1088/1674-1056/abe1a6

Toroidal rotation induced by 4.6 GHz lower hybrid current drive on EAST tokamak

Xiang-Hui Yin(尹相辉), Jun Chen(陈俊), Rui-Ji Hu(胡睿佶), Ying-Ying Li(李颖颖), Fu-Di Wang(王福地), Jia Fu(符佳), Bo-Jiang Ding(丁伯江), Mao Wang(王茂), Fu-Kun Liu(刘甫坤), Qing Zang(臧庆), Yue-Jiang Shi(石跃江), Bo Lyu(吕波), Bao-Nian Wan(万宝年), EAST team
Chin. Phys. B, 2017, 26 (**11**): 115203. DOI: 10.1088/1674-1056/26/11/115203

Optimized calculation of the synergy conditions between electron cyclotron current drive and lower hybrid current drive on EAST

Wei Wei(韦维), Bo-Jiang Ding(丁伯江), Y Peysson, J Decker, Miao-Hui Li(李妙辉),Xin-Jun Zhang(张新军), Xiao-Jie Wang(王晓洁), Lei Zhang(张磊)
Chin. Phys. B, 2016, 25 (**1**): 015201. DOI: 10.1088/1674-1056/25/1/015201

Compound sawtooth in EAST LHCD plasma： An experimental study

Xu Li-Qing, Hu Li-Qun, Chen Kai-Yun, Li Miao-Hui
Chin. Phys. B, 2014, 23 (**8**): 085201. DOI: 10.1088/1674-1056/23/8/085201

Parametric decay instabilities of lower hybrid waves on CFETR

Taotao Zhou(周涛涛)[1,2], Nong Xiang(项农)[1,3,†], Chunyun Gan(甘春芸)[1,3,‡], Guozhang Jia(贾国章)[1,3], and Jiale Chen(陈佳乐)[1,3]

[1] *Institute of Plasma Physics, Hefei Institutes of Physical Science, Chinese Academy of Sciences, Hefei* 230031, *China*
[2] *University of Science and Technology of China, Hefei* 230026, *China*
[3] *Centre of Magnetic Fusion Theory, Chinese Academy of Sciences, Hefei* 230031, *China*

(Received 20 January 2022; revised manuscript received 1 April 2022; accepted manuscript online 18 April 2022)

The lower hybrid current drive is a potential candidate for sustaining plasma current in tokamak steady-state operations, which could be used in China Fusion Engineering Test Reactor (CFETR) with input power up to a few tens of megawatts. Such high input power could trigger the well-known parametric instabilities (PIs) at the plasma edge affecting the propagation and absorption of the lower hybrid pump waves. By analytically solving the nonlinear dispersion relation describing PIs, an explicit expression of the PI growth rate is obtained and analyzed in detail. It is found that pressure is the key parameter determining the PI characteristics. Ion sound quasi-mode is the dominant decay channel in the low-pressure regime, while the ion cyclotron quasi-mode (ICQM), as well as its harmonics, becomes dominant in the intermediate regime. In the high-pressure regime, only one mixed channel is found, which is related to Landau damping by free-streaming ions. Analytical expressions of growth rates of these decay channels are also obtained to show the parameter dependence at different pressure limits. The above analytical results are used to estimate the PIs on a typical profile of CFETR, and verified by corresponding numerical calculations. ICQM is found to be the strongest decay channel with a considerable growth rate for CFETR.

Keywords: lower hybrid, parametric instability, CFETR

PACS: 52.35.Hr, 52.35.Mw, 52.55.Fa **DOI:** 10.1088/1674-1056/ac67c2

1. Introduction

In order to maintain the steady-state operation in a tokamak, a substantial net toroidal plasma current is required.[1,2] Besides the bootstrap current, additional currents should be driven for the flexible control of the current profile.[3] The lower hybrid current drive (LHCD) system has been widely adopted in tokamak due to its high efficiency since the first successful demonstration in the PLT tokamak.[4] Recently, it also became a candidate for sustaining plasma current in operation scenarios of China Fusion Engineering Test Reactor (CFETR), a future bridging device between ITER and DEMO.[5,6] However, in some pioneering LHCD experiments with high densities ($n_e > 0.8 \times 10^{20}$ m^{-3}), sudden loss of fast electrons and current drive efficiency was detected,[7–9] which may also happen on CFETR with higher densities. The phenomenon results from the power depletion at the plasma edge induced by the nonlinear effects of the injected lower-hybrid (LH) wave.[10] One of the most promising mechanisms is the parameter instability (PI).[11]

The PI process describes that a pump wave delivers its energy to two child waves when the pump power exceeds its nonlinear threshold.[10] It has been widely studied since 1970s when it was used to explain the power coupling failure in the LH heating experiments.[12–15] By solving the Vlasov equation under a dipole electric field approximation near the LH frequency, the nonlinear dispersion relation describing the PI process was first established by Porkolab.[16] Based on the results of the dispersion relation and other contemporaneous approaches, various possible decay channels were discussed in different parameter limits.[17] For the LHCD experiments in tokamaks, only two of the decay channels are found to be important.[11] One refers to the child-mode combination of a low-frequency ion cyclotron quasi-mode (ICQM) and an LH sideband with a small frequency shift. It is a possible reason for the observed non-monotonic envelope in the frequency spectra.[18,19] The other is the combination of an ion sound quasi-mode (ISQM) and an LH sideband, which causes the frequency broadening.[10] In the critical work of Cesario *et al.*,[20] the ISQM-type PI was also found to be able to affect the LH deposition process through the spectral broadening on the parallel refractive index $n_\parallel$.

Since an increased temperature or a decreased density was found to be able to reduce PIs of the two decay channels,[21,22] inspiring progress has been made in recovering the LHCD efficiency by mitigating PI in recent high-density experiments. Frascati Tokamak Upgrade (FTU) is the first tokamak achieving high-efficiency LHCD in a line-averaged density of 1.5×10^{20} m^{-3} with PIs suppressed through increasing the edge T_e.[23] In EAST, the LHCD efficiency is recovered by decreasing edge density with strong wall lithiation.[24] In experiments of Alactor-C Mod, efficient LHCD was realized

†Corresponding author. E-mail: xiangn@ipp.ac.cn
‡Corresponding author. E-mail: cygan@ipp.ac.cn

© 2022 Chinese Physical Society and IOP Publishing Ltd

with reduced density shoulders.[25,26]

By extending the experience to CFETR, it can be found that some of its parameter differences from the conventional tokamaks may significantly trigger PI. In Fig. 1, the ranges of n_e and T_e are shown for CEFTR and other PI-relevant tokamaks. It can be seen that the density in reactors (ITER,[27] CFETR,[28] and DEMO[27]) will be higher than the present tokamaks (JET,[29] EAST[30]), which will increase the instability. Meanwhile, the demanded high pump LH power also contributes to PI. However, it should also be noticed that the higher T_e in the reactors can reduce PI. The resulting net effect remains unclear as the sensitivities on n_e and T_e or other parameters have not been compared precisely yet. Thus, the PI on CFETR still requires more thorough investigations.

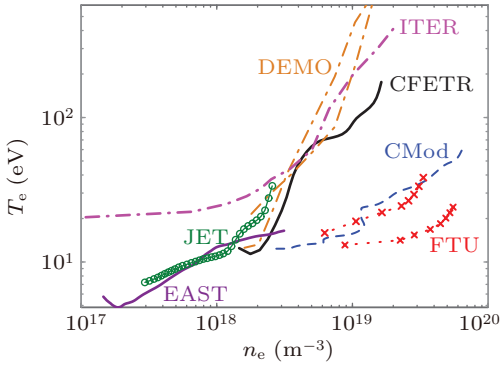


Fig. 1. The n_e–T_e distribution of SOL plasma in Alactor-C Mod,[25] CFETR,[28] DEMO,[27] EAST,[30] FTU,[23] ITER,[27] and JET.[29] These SOL n_e–T_e lines start from the antenna grill and end up at their own separatrix.

To learn the nature of PI in CFETR or other situations with unforeseen parameter sets, understanding the parameter dependence is crucial. Besides a lower n_e and a higher T_e, a lower PI has also been found to be related to a higher magnetic field B_0, a higher pump frequency ω_0, and a higher ion mass based on numerical parameter scanning.[21,22] However, it is still hard to apply the existing conclusion to CFETR as the change of the parameter regime can also affect the parameter dependence. For example, the ICQM growth rate for JET-like parameters increases linearly with n_e,[22,31] while for FT parameters it increases with n_e at a weakening speed.[11] For the density range in the edge regions of JET, EAST and C-Mod, the ISQM growth rate decreases with n_e at low densities ($< 2.0\times10^{18}$ m^{-3}) but increases at high densities.[22] As for the dependence on $n_\parallel$ of the child mode, the growth rate increases with $n_\parallel$ at a low density (2.5×10^{17} m^{-3}), but decreases at a high density (1.0×10^{18} m^{-3}).[29] Therefore, analytical analysis is required for determining the division of parameter regimes. As will be seen in this paper, a key parameter dividing the regimes will be found by analyzing the dispersion relation of the low-frequency mode. The characteristic of each regime will be studied, as well as some possible new decay channels and parameter dependence.

The rest of the paper is organized as follows. The nonlinear dispersion relation we solved is introduced in Section 2. In Section 3, the PI decay channels and parameter dependence in different parameter limits are discussed by analyzing the PI growth rates, while the numerical solutions are also given to verify the validity. In Section 4, the analytical formula is further applied to investigate the PIs on CFETR. Finally, the summary is presented in Section 5.

2. Physical model

The widely used nonlinear dispersion relation, derived by Porkolab in the electrostatic framework with full-kinetic ions and drift-kinetic electrons,[16,18] is applied in this paper to describe the PI process of an LH pump. Here, a homogeneous and collisionless plasma is considered with a magnetic field B_0 in the z direction of Cartesian coordinates. For simplicity, the density and temperature of ions and electrons can be assumed to be the same ($n_i \simeq n_e$, $T_i \simeq T_e$). An LH eigenmode (ω_0, $\boldsymbol{k}_0$) with a high amplitude electric field E_0 oscillates in the plasma as the pump wave, where ω_0 is the angular frequency and $\boldsymbol{k}_0$ is the wave number. The pump wave decays into a low-frequency mode ($\omega, \boldsymbol{k}$) and an LH sideband ($\omega_1, \boldsymbol{k}_1$) or ($\omega_2, \boldsymbol{k}_2$), where the selection rules $\omega_{1,2} = \omega \mp \omega_0$, $\boldsymbol{k}_{1,2} = \boldsymbol{k} \mp \boldsymbol{k}_0$ are satisfied. When the LH sideband ($\omega_1, \boldsymbol{k}_1$) is resonant, the sideband ($\omega_2, \boldsymbol{k}_2$) becomes non-resonant and its contribution is negligible as compared to the resonant one.[32] The dispersion relation based on the above assumptions takes the form

$$\varepsilon - \frac{\mu_1}{\varepsilon_1} = 0, \tag{1}$$

$$\mu_1 = \alpha_1\alpha_3 + \beta_3\varepsilon. \tag{2}$$

Here, ε is the linear dispersion relation of the low-frequency mode and takes the form

$$\varepsilon = 1 + \chi_i + \chi_e, \tag{3}$$

where the susceptibilities χ_i and χ_e can be written as

$$\chi_i = \frac{2\omega_{pi}^2}{k^2 v_{ti}^2}\left[1 + \sum_{n=-\infty}^{\infty} I_n(\lambda_i)e^{-\lambda_i}\frac{\omega_r}{k_z v_{ti}} Z\left(\frac{\omega_r - n\omega_{ci}}{k_z v_{ti}}\right)\right], \tag{4}$$

$$\chi_e = \frac{2\omega_{pe}^2}{k^2 v_{te}^2}\left[1 + \frac{\omega_r}{k_z v_{te}} Z\left(\frac{\omega_r}{k_z v_{te}}\right)\right]. \tag{5}$$

Here, ω_{pj} and v_{tj} are the plasma frequency and thermal velocity of the j-th species, respectively, and $v_{tj} = \sqrt{2T_j/m_j}$. The argument of the n-th bessel function I_n, noted by λ_i, equals $\frac{k_\perp^2 v_{ti}^2}{2\omega_{ci}^2}$, where ω_{ci} is ion cyclotron frequency. Z is the dispersion function.

The linear dispersion relation of the LH sideband ε_1 can be written as a more simple form since its frequency satisfies $\omega_{ci} \ll \omega_1 \ll \omega_{ce}$. It is[33]

$$\varepsilon_1 = 1 + \frac{k_{1\perp}^2}{k_1^2}\frac{\omega_{pe}^2}{\omega_{ce}^2} - \frac{k_{1z}^2}{k_1^2}\frac{\omega_{pe}^2}{\omega_1^2}, \tag{6}$$

with ω_{ce} being the electron cyclotron frequency.

The coupling coefficient α_1 corresponds to the pump-sideband quasi-linear coupling, while α_3 and β_3 denote the quasi-linear and nonlinear coupling, respectively, between the pump and low-frequency mode.[17,31] These coefficients are

$$\alpha_1 = \frac{e}{m_e}\frac{\omega_{pe}^2}{k^2 v_{te}^3}(\omega Z - \omega_0 Z_0 - \omega_1 Z_1) \times \left[-\frac{|\boldsymbol{k}_{1\perp}\times\boldsymbol{E}_{0\perp}|}{\omega_{ce}(\omega k_{0z}-\omega_0 k_z)} - \frac{\mathrm{i}k_z k_{1z}E_{0z}}{(\omega k_{0z}-\omega_0 k_z)^2}\right], \quad (7)$$

$$\alpha_3 = \frac{e}{m_e}\frac{\omega_{pe}^2}{k_1^2 v_{te}^3}(\omega Z - \omega_0 Z_0 - \omega_1 Z_1) \times \left[-\frac{|\boldsymbol{k}_{\perp}\times\boldsymbol{E}^*_{0\perp}|}{\omega_{ce}(\omega_1 k_{0z}-\omega_0 k_{1z})} + \frac{\mathrm{i}k_{1z}k_z E^*_{0z}}{(\omega_1 k_{0z}-\omega_0 k_{1z})^2}\right], \quad (8)$$

$$\beta_3 = \frac{e}{m_e}\frac{k^2}{2k_1^2}\left[-\frac{|\boldsymbol{k}_{1\perp}\times\boldsymbol{E}^*_{0\perp}|}{\omega_{ce}\omega_1} + \frac{\mathrm{i}k_{1z}E^*_{0z}}{\omega_1^2}\right]\alpha_1. \quad (9)$$

Here, e and m_e are the electron charge and mass, respectively. Z_m represents the dispersion function of the m-th mode with the argument $\frac{\omega_m}{k_{mz}v_{te}}$. The superscript * represents the complex conjugation.

Low-order terms with respect to ω_0^2/ω_{ce}^2 in these coupling coefficients are neglected as the LH frequency is much lower than ω_{ce}. In the square bracket of α_1, the first term represents the coupling effect from the $\boldsymbol{E}_{0\perp}\times\boldsymbol{B}_0$ drift motion of electrons, while the second term results from the electron motion parallel to $\boldsymbol{B}_0$.

3. PI in different parameter regimes

3.1. Key parameter determining the characteristics of PI

Considering a complex sideband frequency $\omega_1 \simeq \omega_{1r} + \mathrm{i}\gamma_1$ with $\gamma_1 \ll \omega_{1r}$ for weak damping or growth, Eq. (1) can be rewritten as an expression of the sideband growth rate $\gamma_1 = \frac{\mathrm{Im}(\mu_1/\varepsilon)}{\partial\varepsilon_{1r}/\partial\omega_{1r}}$ and the nonlinear part γ^{NL}, i.e., the growth rate of the PI process.[17] Assuming that the LH sideband is not a damping mode ($\gamma_{1L} \simeq 0$), the PI growth rate becomes

$$\gamma^{NL} \approx \frac{e^2 P_0 N_{0z}}{2\varepsilon_0 S m_e^2 c v_{te}^2}\mathrm{Im}\left(\frac{\kappa_i\kappa_e}{\kappa_i+\kappa_e}\right)\left(\frac{\omega_{pe}^3}{\omega_{ce}^2\omega_0^2}+\frac{1}{\omega_{pe}}\right). \quad (10)$$

For the detailed derivation and approximations one can see Appendix A. Here, P_0 is the pump power and S denotes the cross-sectional area of the LH antenna mouth. N_{0z} is the parallel refractive index; c is the light speed in vacuum, and ε_0 is the dielectric constant. The first term in the second bracket on the right-hand side of Eq. (10) corresponds to the drift coupling term driven by $\boldsymbol{E}_{0\perp}$ in Eqs. (7) and (8), where $k_{1\perp}$ has been chosen to be perpendicular to $k_{0\perp}$ to maximize this coupling term. The second term is the parallel coupling term driven by E_{0z}.

Here, κ_j is part of the susceptibility of the j-th species, and it is defined as

$$\kappa_j = \frac{k^2 v_{tj}^2}{2\omega_{pj}^2}\chi_j. \quad (11)$$

Since ω_r's for the ISQM and ICQMs are below or at the level of several ω_{ci}, a value much lower than $k_z v_{te}$, then the term with dispersion function Z in Eq. (5) is neglected and κ_e here can be approximated as 1. The susceptibility term then reduces to $\frac{\mathrm{Im}(\kappa_i)}{[1+\mathrm{Re}(\kappa_i)]^2+\mathrm{Im}(\kappa_i)^2}$. Obviously, the dominator $\mathrm{Im}(\kappa_i)$ plays an important role in determining the growth rate. Using Eq. (4), we can reach

$$\mathrm{Im}(\kappa_i) = \sqrt{\pi}\sum_{n=-\infty}^{\infty}\frac{\omega_r}{k_z v_{ti}} I_n(\lambda_i)\mathrm{e}^{-\lambda_i}\mathrm{e}^{-\frac{(\omega_r - n\omega_{ci})^2}{k_z^2 v_{ti}^2}}, \quad (12)$$

and we will discuss it in different limits of its parameter λ_i.

When $\lambda_i \ll 1$, only the first few terms in Eq. (12) contribute to $\mathrm{Im}(\kappa_i)$, which can be simplified to

$$\mathrm{Im}(\kappa_i) \approx \sqrt{\pi}\frac{\omega_r}{k_z v_{ti}}\left[(1-\lambda_i)\mathrm{e}^{-\frac{\omega_r^2}{k_z^2 v_{ti}^2}} + \frac{1}{2}\lambda_i \mathrm{e}^{-\frac{(\omega_r-\omega_{ci})^2}{k_z^2 v_{ti}^2}}\right]. \quad (13)$$

The left and right exponential terms in the square bracket correspond to ISQM with $\omega_r \approx k_z v_{ti}$ and ICQM with $\omega_r \approx \omega_{ci} + k_z v_{ti}$, respectively. Here, the ISQM term is in the order of 1, and the ICQM term is in the order of λ_i, suggesting that the ISQM is much stronger than ICQM in this limit.

For $\lambda_i \geq 1$, the $\mathrm{Im}(\kappa_i)$ can be derived using the expression of κ_i from Brambilla,[34]

$$\mathrm{Im}(\kappa_i) \approx \frac{\omega_r}{k v_{ti}}\mathrm{e}^{-\frac{\omega_r^2}{k^2 v_{ti}^2}}\sum_{n=0}^{5\sqrt{\lambda_i}}\frac{\omega_{ci}}{k_z v_{ti}}\mathrm{e}^{-\frac{(\omega_r - n\omega_{ci})^2}{k_z^2 v_{ti}^2}}. \quad (14)$$

The exponential terms in the summation with $n = 0 \sim 5\sqrt{\lambda_i}$ correspond to ISQM and several ICQM harmonics, where the maximum number of the ICQM harmonics is the integer around $5\sqrt{\lambda_i}$, and $n = 0$ represents the ISQM. This implies that more ICQM harmonics will be excited as the λ_i increases further. The strongest decay channel among them satisfies $n\omega_{ci} = k v_{ti}$.

For $\lambda_i \gg 1$, where the temperature is also high enough that $k_z\rho_i \geq 1$ (ρ_i refers to the ion Larmor radius, equal to v_{ti}/ω_{ci}), the summation in Eq. (14) can be taken as an integral and equals $\sqrt{\pi}$. Then $\mathrm{Im}(\kappa_i)$ becomes

$$\mathrm{Im}(\kappa_i) \approx \sqrt{\pi}\frac{\omega_r}{k v_{ti}}\mathrm{e}^{-\frac{\omega_r^2}{k^2 v_{ti}^2}}. \quad (15)$$

Since the ion Larmor radius here is much larger than the wavelength ($k_\perp\rho_i = \sqrt{2\lambda_i} \gg 1$), the ions stream almost freely within a wavelength, thus absorb the wave energy through only the ion Landau damping, as described by Glagolev.[35] In the perspective of PI, Eq. (15) shows only one decay channel, of which the maximum value locates near $\omega_r = k v_{ti}$, somewhere different from ISQM and ICQM.

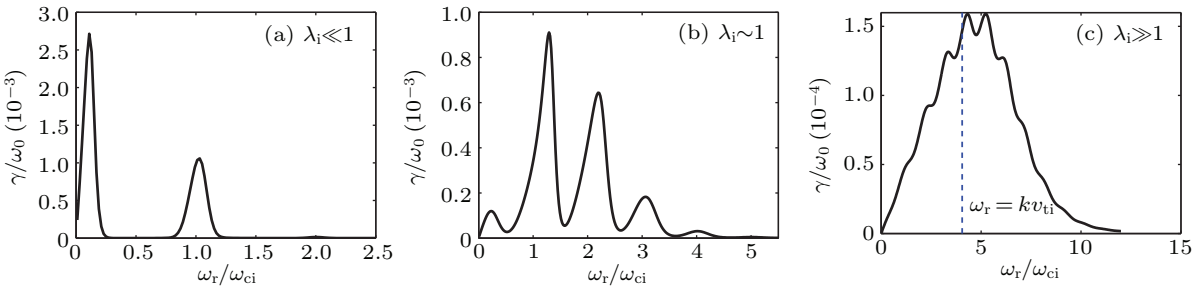


Fig. 2. Normalized numerical growth rate γ/ω_0 (black solid lines) versus the normalized real frequency of the low frequency mode ω_r/ω_{ci} with typical parameter sets for different λ_i limits: (a) $\lambda_i = 0.024$; (b) $\lambda_i = 0.99$, $k_z\rho_i = 0.26$; (c) $\lambda_i = 8.0$, $k_z\rho_i = 0.6$. The blue dashed line in (c) notes the peak location derived from Eq. (15).

To understand these expressions in different limits of λ_i more intuitively, especially the unclear decay channel implied by Eq. (15), numerical studies are also performed by solving Eq. (1). The detailed solving process for accessing the numerical PI growth rates in this paper follows Ref. [22]. Figure 2 shows the ω_r spectra of the numerical PI growth rates under three different λ_i limits. For the case of $\lambda_i \ll 1$ shown by Fig. 2(a), two unstable regions are found. They locate at $\omega_r \ll \omega_{ci}$ and $\omega_r \approx \omega_{ci}$, which obviously correspond to the ISQM and ICQM, respectively. ISQM here is much stronger than ICQM. In Fig. 2(b) ($\lambda_i \sim 1$), up to 4 unstable modes are found, which are actually ISQM and ICQM harmonics. ICQMs here are much stronger than ISQM. In Fig. 2(c), when $\lambda_i \gg 1$ and $k_z\rho_i$ approaches 1, the ICQM harmonics can be still observed from the peaks near $\omega_r \approx n\omega_{ci}$. Compared with Fig. 2(b), these ICQMs overlap seriously, and look rather like a single peak with maximum value at $\omega_r = kv_{ti}$. In this sense, the decay channel seems to be a special form of the ICQMs. From the analysis of Eqs. (14) and (15), it should also be noticed that the ion damping has changed from the cyclotron damping to the Landau damping during the overlapping. Therefore, we should regard the peak as a new decay channel driven by the nonlinear ion Landau damping (NILD) rather than the simple overlapping of the ICQMs.

Now it is learnt that λ_i is the key parameter characterizing PI decay channels and growth rate. In fact, this parameter is directly related to the plasma pressure $p = en_iT_i + en_eT_e \simeq 2en_eT_e$ (T_i and T_e here are in units of eV). Using the approximated dispersion relation $\frac{k_{0\perp}^2}{k_{0z}^2} \approx \frac{k_{1\perp}^2}{k_{1z}^2} \approx \frac{\omega_{pe}^2}{\omega_0^2}$ for the edge plasma ($\omega_{pe} \ll \omega_{ce}$), $\lambda_i = \frac{k_\perp^2 v_{ti}^2}{2\omega_{ci}^2}$ can be approximated as $\frac{N_{0z}^2+N_{1z}^2}{m_e/m_i}\frac{en_eT_i}{B_0^2/\mu_0}$. The relation between λ_i and p is

$$\lambda_i = \frac{N_{0z}^2+N_{1z}^2}{4m_e/m_i}\frac{p}{p_B}, \tag{16}$$

where $p_B = B_0^2/2\mu_0$ is the magnetic pressure (μ_0 is the permeability of the free space).

Essentially, it is the plasma pressure p determining the PI decay channels, and p will be the key parameter in the following discussion on PI parameter dependence. To give a clear division of different pressure regimes, a critical pressure p^{crit} is defined using $\lambda_i = 1$, and

$$p^{crit} = \frac{4m_e/m_i}{N_{0z}^2+N_{1z}^2}p_B. \tag{17}$$

The dependence on pressure can then be concluded as follows. When $p \ll p^{crit}$, it is the low-pressure regime and there are only ISQM and fundamental ICQM. When $p \gg p^{crit}$, it is the high-pressure regime and the NILD decay channel takes effect. For the intermediate regime, i.e., $p \sim p^{crit}$, decay channels of multiple ICQM harmonics are found.

3.2. Low-pressure regime

As mentioned in the last subsection, ISQM and fundamental ICQM are the main decay channels of this regime. By substituting the corresponding characteristic real frequencies ($\omega_r = k_z v_{ti}$ for ISQM, $\omega_r = \omega_{ci} + k_z v_{ti}$ for ICQM) into Eqs. (10) and (13), we can obtain the analytical growth rates of the two decay channels. For clarity and direct use, they are written in explicit forms with respect to the parameters.

$$\gamma^{ISQM} \approx \frac{0.128e^2}{\varepsilon_0^{2.5}m_e^{0.5}c}P_0N_{0z}S^{-1}T_e^{-1}\left(1-1.89p/p^{crit}\right) \times \left(n_e^{1.5}B_0^{-2}\omega_0^{-2} + \frac{\varepsilon_0^2}{e^2}n_e^{-0.5}\right), \tag{18}$$

$$\gamma^{ICQM} \approx \frac{0.058\mu_0 e^{3.5}m_i}{\varepsilon_0^{2.5}m_e^{1.5}}P_0N_{0z}S^{-1}N_zT_e^{-0.5}\mathrm{F}\left(p/p^{crit}, k_z\rho_i\right) \times \left(n_e^{2.5}B_0^{-3}\omega_0^{-3} + \frac{\varepsilon_0^2}{e^2}n_e^{-0.5}B_0^{-1}\omega_0^{-1}\right), \tag{19}$$

where

$$F(x_1,x_2) = \frac{(1-x_1)(1+x_2)}{1+0.42x_1-1.08x_1x_2^{-1}+0.40x_1^2x_2^{-2}}.$$

The terms in the first bracket of Eqs. (18) and (19) result from the susceptibility terms, which depend heavily on the pressure. According to Eq. (18), a higher pressure can stabilize ISQM. Since F in Eq. (19) is an increasing function with respect to p/p^{crit}, higher pressure may lead to higher ICQM growth rate. In the low-pressure limit, clear parameter dependence can be obtained by rewriting Eqs. (18) and (19) to the lowest order of p/p^{crit}.

$$\gamma^{ISQM} \propto T_e^{-1}\left(n_e^{1.5}B_0^{-2}\omega_0^{-2} + \frac{\varepsilon_0^2}{e^2}n_e^{-0.5}\right), \tag{20}$$

$$\gamma^{\mathrm{ICQM}} \propto N_z T_\mathrm{e}^{-0.5}\left(n_\mathrm{e}^{2.5}B_0^{-3}\omega_0^{-3}+\frac{\varepsilon_0^2}{e^2}n_\mathrm{e}^{-0.5}B_0^{-1}\omega_0^{-1}\right), \quad (21)$$

where the parameters with stable dependence such as P_0 and S have been omitted.

For the low-pressure regime, there must be a low density limit ($n_\mathrm{e} \ll \frac{\varepsilon_0}{e}B_0\omega_0$), where the E_{0z} coupling term dominates. The dependence can reduce to

$$\gamma^{\mathrm{ISQM}} \propto n_\mathrm{e}^{-0.5}T_\mathrm{e}^{-1}, \quad (22)$$

$$\gamma^{\mathrm{ICQM}} \propto N_z n_\mathrm{e}^{0.5}T_\mathrm{e}^{-0.5}B_0^{-1}\omega_0^{-1}. \quad (23)$$

It can be found that the parameter dependence of ISQM is quite simple with only n_e and T_e involved, so that the ISQM is almost independent of N_z, B_0 and ω_0. It indicates that the ISQM growth rate can be reduced by a higher n_e or a higher T_e while the latter is more effective in mitigating ISQM-type PI. An increasing T_e, B_0, or ω_0 can all reduce the ICQM growth rate, except for an increasing n_e.

One may also find a high density limit in this regime if ($n_\mathrm{e} \gg \frac{\varepsilon_0}{e}B_0\omega_0$), where the $E_{0\perp}\times B_0$ coupling term dominates. Then the parameter dependence is

$$\gamma^{\mathrm{ISQM}} \propto n_\mathrm{e}^{1.5}T_\mathrm{e}^{-1}B_0^{-2}\omega_0^{-2}, \quad (24)$$

$$\gamma^{\mathrm{ICQM}} \propto N_z n_\mathrm{e}^{2.5}T_\mathrm{e}^{-0.5}B_0^{-3}\omega_0^{-3}. \quad (25)$$

In a qualitative aspect, the dependence in this regime agrees well with the published works.[21,22] Quantitatively, the present results can additionally show the sensitivities to the parameter through their powers in the equations. For example, ISQM is more sensitive to T_e than ICQM in both density limits. In the high density limit, ISQM also increases with n_e, but with a rather slower speed than ICQM.

In Fig. 3, the dependence of growth rates predicted by Eqs. (20) and (21) on n_e and T_e are plotted, together with the corresponding numerical growth rates as verification. The numerical growth rate of a decay channel indicates the peak growth rate of the corresponding unstable region similar to that shown in Fig. 2. Consequently, most of the numerical growth rates agree with the analytical trends. In Fig. 3(a), the analytical trend of ISQM grows slightly slower than the numerical growth rate because the finite effect of the term $1-1.89p/p^{\mathrm{crit}}$ in Eq. (18) not included.

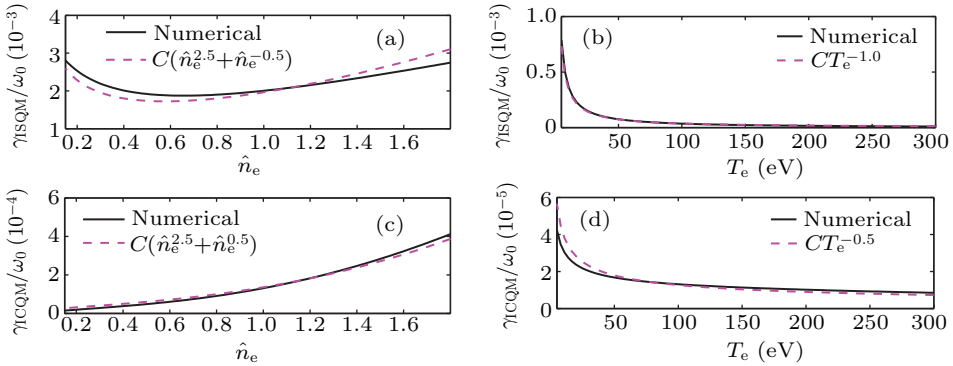


Fig. 3. The trends of ISQM and ICQM growth rates (purple dashed lines) on n_e [(a), (c)] and T_e [(b), (d)] predicted by Eqs. (20) and (21). Here p/p^{crit} is in the range of 0.01–0.2, a typical value for the low-pressure regime. In (a) and (c), the $\hat{n}_\mathrm{e}$ is the normalized to the critical density $\frac{\varepsilon_0}{e}B_0\omega_0$ to show whether the range is in the low density or high density limit. Here, the effects of both density limits are included since $\hat{n}_\mathrm{e}$ is 0.15–1.8. As verification, the corresponding numerical parameter dependence of ISQM and ICQM growth rates (black solid lines) is also plotted. For better comparison, the constants of the analytical lines (C in the legends) are chosen as the mean values of the numerical lines.

3.3. High-pressure regime

In the high density regime, only the NILD decay channel can be found. As illustrated in Eq. (13), the ion susceptibility here is independent of p/p^{crit}. The characteristic frequency of NILD is $\omega_\mathrm{r} = 1.17k_z v_{\mathrm{ti}}$, where susceptibility term reaches its maximum value. Therefore, the growth rate of NILD can be derived as

$$\gamma^{\mathrm{NILD}} \approx \frac{0.146e^2}{\varepsilon_0^{2.5}m_\mathrm{e}^{0.5}c}P_0N_{0z}S^{-1}T_\mathrm{e}^{-1} \times\left(n_\mathrm{e}^{1.5}B_0^{-2}\omega_0^{-2}+\frac{\varepsilon_0^2}{e^2}n_\mathrm{e}^{-0.5}\right). \quad (26)$$

The expression can also be used for quick estimation on growth rate like Eqs. (18) and (19). In the high density limit for the high pressure, the parameter dependence is

$$\gamma^{\mathrm{NILD}} \propto n_\mathrm{e}^{1.5}T_\mathrm{e}^{-1}B_0^{-2}\omega_0^{-2}. \quad (27)$$

In the low density limit, which requires $n_\mathrm{e} \ll \frac{\varepsilon_0}{e}B_0\omega_0$, the dependence is

$$\gamma^{\mathrm{NILD}} \propto n_\mathrm{e}^{-0.5}T_\mathrm{e}^{-1}. \quad (28)$$

It can be easily seen that the parameter dependence of NILD is the same as the ISQM in the low-pressure limit, because both of their susceptibility terms are almost irrelevant to the ion cyclotron motion and then contribute nothing to the dependence. For ISQM, only the ion motion parallel to B_0 is considered. For NILD, the ions move approximately in a straight line within a wavelength of the low-frequency mode as it is much shorter than the Larmor radius.

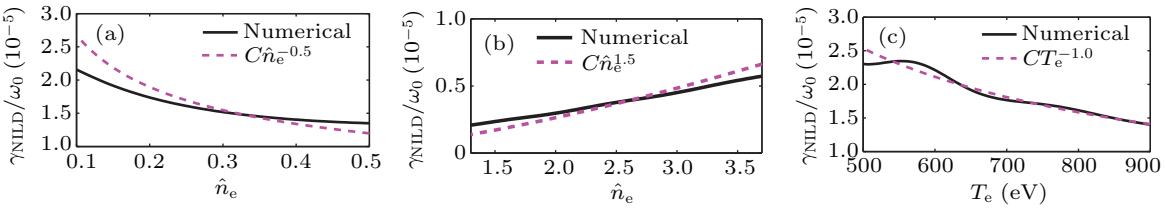


Fig. 4. Similar to Fig. 3, the analytical trends (purple dashed lines) on n_e and T_e predicted by Eqs. (27) and (28), compared with the corresponding numerical NILD growth rates (black lines). Here, p/p^{crit} is in the range of 6–20; $k_z\rho_i$ is in the range of 0.6–1.9, typical for the high-pressure regime. [(a), (b)] Dependence on n_e in the low and high density limits, respectively. (c) Dependence on T_e.

For the high-pressure regime, the trend predictions from Eqs. (27) and (28) are also compared with the numerical parameter dependence in Fig. 4. It can be seen that the trends agree with the numerical results, except for some subtle jitters on the numerical lines in Fig. 4(c). The jitters are attributed to insufficient overlapping of the ICQM harmonics as shown by Fig. 2(c). They will vanish when T_e further rises.

3.4. Intermediate regime

Since there does not exist proper parameter limit of λ_i in the intermediate regime, it is difficult to find a proper approximation for the susceptibility term and to directly show the explicit forms of growth rates. Instead, this regime is studied based on some rough analysis of the dependence on λ_i. In Fig. 5, the susceptibility terms of various decay channels are plotted as functions of λ_i. For ISQM, the susceptibility term decreases monotonously with the increase of λ_i, and finally loses to the ICQMs in the intermediate regime ($\lambda_i > 0.5$). We will no longer take it into account in this subsection. Unlike ISQM, the ICQMs first increase and then decrease with λ_i, and take turns to dominate in the order of n. Therefore, for nth ICQM harmonic, there always exists an interval of λ_i (usually locates in the vicinity of $\lambda_i \simeq n$), where the susceptibility term reaches its peak value and changes slowly with λ_i. Based on this characteristic, in the vicinity of the peak value, the relation of $\mathrm{Im}\left(\frac{\kappa_i\kappa_e}{\kappa_i+\kappa_e}\right)$ to λ_i can be considered to change from $\lambda_i^{0.5}$ to $\lambda_i^{-0.5}$ with the increase of λ_i, namely,

$$\mathrm{Im}\left(\frac{\kappa_i\kappa_e}{\kappa_i+\kappa_e}\right)^{\mathrm{ICQMn}} \propto \frac{\lambda_i^{0.5}}{k_z\rho_i} \to \frac{\lambda_i^{0}}{k_z\rho_i} \to \frac{\lambda_i^{-0.5}}{k_z\rho_i} \quad \text{for} \quad \lambda_i \approx n. \tag{29}$$

Here, we use $\to$ to link the change of the parameter dependence due to the increase of λ_i. For the low density limit, using the above relation, the parameter dependence takes the form

$$\gamma^{\mathrm{ICQMn}} \propto T_e^{-1}\omega_0^{-1} \to N_z^{-1}n_e^{-0.5}T_e^{-1.5}B_0\omega_0^{-1} \to N_z^{-2}n_e^{-1}T_e^{-2}B_0^2\omega_0^{-1}. \tag{30}$$

For the high density limit, it is

$$\gamma^{\mathrm{ICQMn}} \propto n_e^2T_e^{-1}B_0^{-2}\omega_0^{-3} \to N_z^{-1}n_e^{1.5}T_e^{-1.5}B_0^{-1}\omega_0^{-3} \to N_z^{-2}n_eT_e^{-2}\omega_0^{-3}. \tag{31}$$

The dependences on n_e and B_0 shown in Eq. (30) are quite different from the present knowledge. Under the effect of E_{0z} coupling term, an increasing n_e or a decreasing B_0 no longer strengthens the growth rates of the ICQMs but decreases them instead. Actually, such a trend holds in a very finite parameter range. As the density increases further, the effect of the $\boldsymbol{E}_{0\perp} \times B_0$ term will take in charge, and the dependences on n_e and B_0 are then recovered as described by Eq. (31).

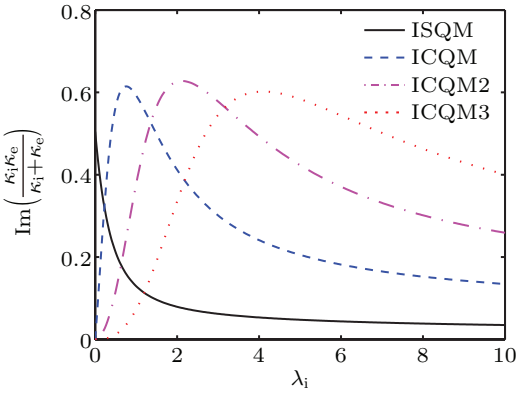


Fig. 5. The susceptibility term $\mathrm{Im}\left(\frac{\kappa_i\kappa_e}{\kappa_i+\kappa_e}\right)$ versus λ_i. Here, κ_i is in a complete form of Eq. (12), $k_z\rho_i$ is fixed at a typical value of 0.3.

According to the relation $T_e^{-1} \to T_e^{-1.5} \to T_e^{-2}$ in both density limits, a low T_e is found to be more capable of reducing the growth rate as the pressure increases. The dependence on n_z changes in a similar way to that on T_e. A higher ω_0 can always decrease the ICQM growth rate here, and it is more effective in the high density limit.

In Fig. 6, similarly, the analytical and numerical parameter dependences in the intermediate regime are compared. The analytical trends are predicted by the middle part of Eqs. (30) and (31), which describe immediate dependences in a finite region where the term $\mathrm{Im}\left(\frac{\kappa_i\kappa_e}{\kappa_i+\kappa_e}\right)$ gets its peak value. It should be noticed that the peak region varies as the harmonic order of ICQM changes, as described in Fig. 5. It can be found that the analytical trends agree with the numerical results in the vicinity of the labeled critical pressure (blue dashed lines). However, the agreements are also possible to fail at positions far from critical ones. In Figs. 6(a) and 6(d), the disagreement found at $\hat{n}_e < 0.2$ indicates a potential increasing trend on n_e for a lower pressure, which follows the description of the left part of Eq. (30). In Figs. 6(b) and 6(e), the failure of the ana-

lytical ICQM when $\hat{n}_e$ is higher than 3.0 is due to the dependence on n_e that is weakened as the pressure further increases. The dependence can be illustrated by the right part of Eq. (31). The disagreement found in the low T_e in Fig. 6(f) corresponds to the change of parameter dependence due to lower pressure as described by Eq. (23).

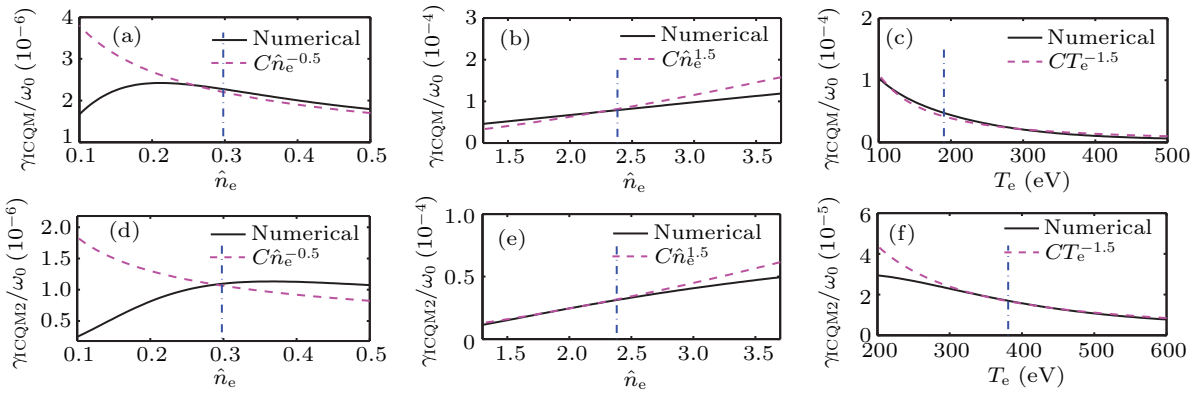


Fig. 6. Similar to Fig. 3, the analytical trends of ICQM and its secondary harmonic (ICQM2) predicted by the middle parts of Eqs. (30) and (31) are shown as purple dashed lines, while the relevant numerical growth rates are shown as black solid lines for comparison. All the scans are performed around $p/p^{crit} = 1$ for ICQM, and $p/p^{crit} = 2$ for ICQM2, referring to the parameter range of the intermediate regime. The positions with the critical pressure p^{crit} ($2p^{crit}$ for ICQM2) are labeled with blue dot-dashed lines. The dependence on n_e in the low density limit is shown in (a) and (d), while in the high density limit shown in (b) and (e). [(c), (f)] The trends on T_e.

Table 1. Summary of the parameter dependence of PI growth rates in different density limits and pressure regimes.

	Low density limit	High density limit
Low-pressure regime $p \ll p^{crit}$	$\gamma^{ISQM} \propto n_e^{-0.5} T_e^{-1}$ $\gamma^{ICQM} \propto N_z n_e^{0.5} T_e^{-0.5} B_0^{-1} \omega_0^{-1}$	$\gamma^{ISQM} \propto n_e^{1.5} T_e^{-1} B_0^{-2} \omega_0^{-2}$ $\gamma^{ICQM} \propto N_z n_e^{2.5} T_e^{-1} B_0^{-3} \omega_0^{-3}$
Intermediate regime $p \sim np^{crit}$; $k_z\rho_i \ll 1$	$\gamma^{ICQMn} \propto \begin{cases} T_e^{-1}\omega_0^{-1} & \downarrow \\ N_z^{-1} n_e^{-0.5} T_e^{-1.5} B_0 \omega_0^{-1} & \downarrow \\ N_z^{-2} n_e^{-1} T_e^{-2} B_0^2 \omega_0^{-1} & \end{cases}$	$\gamma^{ICQMn} \propto \begin{cases} n_e^2 T_e^{-1} B_0^{-2} \omega_0^{-3} & \downarrow \\ N_z^{-1} n_e^{1.5} T_e^{-1.5} B_0^{-1} \omega_0^{-3} & \downarrow \\ N_z^{-2} n_e T_e^{-2} \omega_0^{-3} & \end{cases}$
High-pressure regime $p \gg p^{crit}$; $k_z\rho_i \geq 1$	$\gamma^{NILD} \propto n_e^{-0.5} T_e^{-1}$	$\gamma^{NILD} \propto n_e^{1.5} T_e^{-1} B_0^{-2} \omega_0^{-2}$

Based on the above discussions, the parameter dependence varying with pressure regime, density limits, and decay channels is then summarized in Table 1. The importance of a proper division of the parameter regimes is now reflected, because significantly different parameter dependence is found among different regimes. An increasing n_e can make ISQM suppressed in the low-pressure regime, but help to enhance NILD in the high-pressure regime. ICQMs in the intermediate regimes decrease with n_e in low density limit but increase with n_e in the high density limit. An increasing T_e can always inhibit PIs in all the pressure regimes, but the efficiency varies. The growth rate of the fundamental ICQM is proportional to $T_e^{-0.5}$ in the low-pressure regime, but decays rather faster in the order of T_e^{-2} in the intermediate regime. A higher B_0 can lower the ICQM growth rate in most cases, but it is also possible to strengthen ICQM if a low density limit is found in the intermediate regime.

In the next section, the theory is applied in PI estimation for the typical profile of CFETR hybrid scenario. The radial profile will be divided into regimes representing different dominant decay channels and parameter dependence. To observe the validity of the analytical descriptions, numerical growth rates will also be calculated by scanning with point-by-point parameters.

4. PIs in the hybrid scenario of CFETR

4.1. Division of pressure regimes on the CFETR profile

Here, a typical set of CFETR edge parameters is studied. The density and temperature distributions along the radial direction are shown in Fig. 7(a). These data are extracted from a set of typical CFETR edge data for the hybrid scenario, which is provided by Chen *et al.*[28] The toroidal magnetic field at the plasma core is $B_t = 6.5$ T, and the magnetic field at the low-field-side edge is around 5 T. As for the ions, pure deuterium gas is used for the numerical setup ($m_i/m_e = 3672$). Following the last section, the density and temperature of ions are assumed the same as electrons. A 4.6 GHz 10 MW LH pump is injected into the plasma with a nominal n_{0z} at 1.7.[36] The antenna cross section is set perpendicular to the radial axis. Its area S is assumed to be 1 m^2.

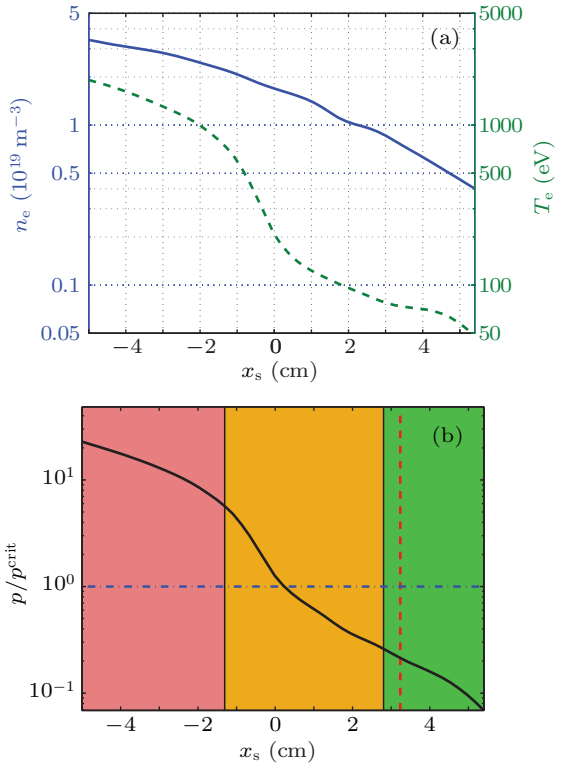


Fig. 7. (a) The plasma density (blue solid line) and temperature (green dashed line) distribution near the separatrix at the outer mid-plane. The radial position x_s is the distance from the separatrix. Negative values of x_s are inside the separatrix. (b) The radial profile of the normalized pressure p/p^{crit} and the division of the pressure regimes. The green area is the low-pressure regime, while the yellow area refers to the intermediate regime and the red area is the high-pressure regime. The blue dot-dashed line corresponds to the critical pressure. The red dashed line marks where the values of $\boldsymbol{E}_{0\perp} \times B_0$ term and E_{0z} term are equal, $n_e = \frac{\varepsilon_0}{e} B_0 \omega_0$, and neither of them could be neglected in the vicinity.

Considering a smooth convective growth in the inhomogeneous plasma,[29,37] the parallel refractive index of the sideband n_{1z} is chosen as a low value of 3. Then in Fig. 7(b), the corresponding pressure distribution of CFETR in shown. It can be seen that the critical pressure locates just near the separatrix. Hence, the outer part of the SOL corresponds to the low-pressure regime. The region of $x_s = -1 \sim 3$ cm belongs to the intermediate regime, while the high-pressure regime distributes inside the separatrix.

4.2. Growth rates as functions of radial positions

In Fig. 8, numerical growth rates of various decay channels are shown as a function of x_s. We can see that from the outside of the separatrix to the inside of the separatrix, the most unstable decay channel changes in the order of ISQM, ICQM, ICQM2, and finally NILD. ISQM is the strongest decay channel at the far edge of $x_s > 4.5$ cm, while ICQM dominates at most parts of the SOL ($x_s = 0 \sim 4.5$ cm). The ICQM2 dominates within a centimeter inside the separatrix ($x_s = -1 \sim 0$ cm), and NILD becomes the major decay channel at $x_s = -4 \sim -1$ cm. The radial distributions of the dominant decay channels agree with the division of the parameter regimes shown in Fig. 7(b). Among the shown decay channels, the ICQM has the maximum growth rate near the position where the p^{crit} locates. The maximum growth rate is $1.6 \times 10^{-3} \omega_0$, which is a value slightly lower than the growth rates found in conventional tokamaks,[24,25,29] implying that comparable PI can also be found in a CFETR-like plasma edge.

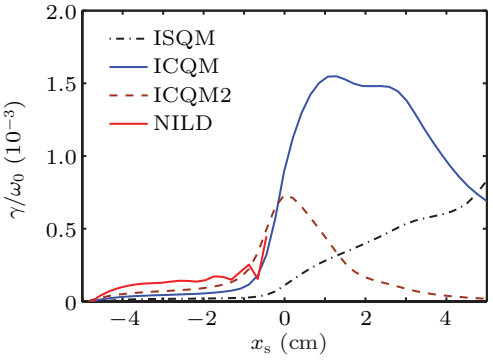


Fig. 8. The distribution of the numerical growth rates on the radial profile for different decay channels, including ISQM (black dot-dash), ICQM (blue solid), ICQM2 (brown dot-dash) and NILD (red-solid). The growth rate of a decay channel is the maximum growth rate scanning the vicinity of the characteristic frequency.

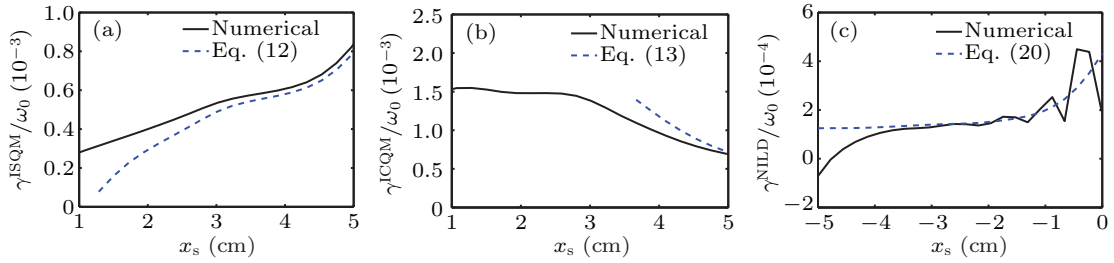


Fig. 9. The growth rates versus x_s, showing the comparison between the numerical growth rates extracted from Fig. 8 and the corresponding analytical approximations. (a) Comparison between the numerical ISQM growth rate and Eq. (18). (b) Numerical ICQM growth rate compared with Eq. (19). (c) Numerical NILD growth rate compared with Eq. (26).

Notice that Eqs. (18), (19) and (26) are explicit expressions of growth rates, which can be used for PI estimation by directly substituting the parameters. In Fig. 9, the applicability of these equations are checked by comparing their results on the profile with the numerical ones which have been shown in Fig. 8. In Figs. 9(a) and 9(b), the analytical growth rates of ISQM and ICQM in the low-pressure regime are checked. It can be found that Eqs. (18) and (19) agree well with the numerical black line at $x_s > 3$ cm, and fail when x_s is lower than 3 cm. Similarly, in Fig. 9(c), the NILD growth rate

in the high-pressure regime is checked. It is almost valid at -4 cm$< x_s < -1$ cm, and fails elsewhere. The disagreement at $x_s < -4$ cm is attributed to electron absorption in high T_e, which is not included in the analytical growth rates.

4.3. Effects of N_z, B_0, and ω_0

Finally, let us discuss the effect of other PI-relevant parameters such as N_z, B_0, and ω_0 briefly. Actually, these parameters can not only affect PI through the previously discussed parameter dependence, but also change the division of the pressure regimes. For example, according to the definition of $p^{\rm crit}$, a higher N_{1z} contributes to a lower $p^{\rm crit}$, and then the low-pressure area shrinks. It can be found from Fig. 10(a) that in a high N_{1z} equal to 6, the low-pressure regime has been extruded out of the present profile. A higher B_0 can increase the $p^{\rm crit}$ and stretch the low-pressure regime and intermediate regime. Thus, in Fig. 10(b), when B_0 is in a higher value of 9 T, the low-pressure regime has occupied a wider profile from the antenna mouth to 0.5 cm, and the high-pressure regime is not found near the SOL. A high ω_0 may not influence $p^{\rm crit}$, but can compress the intermediate region, as the critical temperature between the intermediate and high-pressure regime is an inverse function of ω_0, viz., $T_e^{\rm crit} \propto \frac{B_0^2}{N_z^2\omega_0^2}$.

In Figs. 10(d)–10(f), the radial distribution of the numerical growth rates is plotted correspondingly. The distribution of dominant decay channels almost follows the division of parameter regime shown in Figs. 10(a)–10(c). Furthermore, comparing the numerical results in Fig. 10 with the original results in Fig. 8, we can see that the change in the numerical growth rates also follows the analytical predictions. Since the ISQM growth rate in the low-pressure regime can hardly be affected by neither N_z and B_0 nor ω_0, their results in all subfigures are almost unchanged. According to Eq. (21), ICQM growth rate in the low-pressure regime increases with N_z and decreases with B_0 and ω_0. Correspondingly, it is stronger in Fig. 10(d) and stabilized in Figs. 10(e) and 10(f).

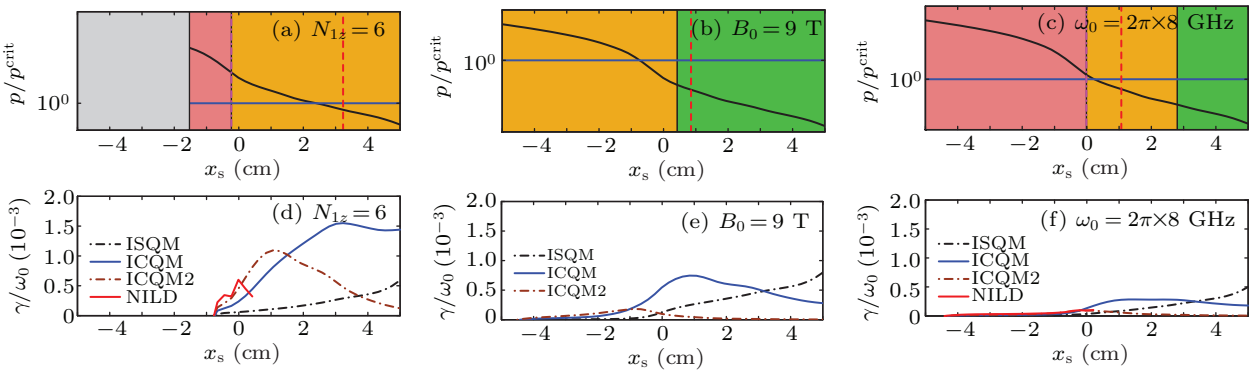


Fig. 10. The division of the parameter regimes and the corresponding numerical growth rates affected by [(a), (d)] a higher N_{1z} at 6, [(b), (e)] a higher B_0 at 9 T and [(c), (f)] a higher ω_0 at 8 GHz. Parameters used here are the same as those in Fig. 7 except the changed one. The gray zones found in (a) refer to stable regions where the sidebands are strongly damped by electrons.

5. Discussion and conclusions

PI is a ubiquitous phenomenon found in LHCD process near plasma edge with low electron temperature. For a reactor level tokamak like CFETR, the onset of PI may be a serious issue affecting the LHCD efficiency as it has higher edge densities and higher pump LH power. In this paper, the nonlinear dispersion relation is analytically and numerically solved to understand the PI effects in CFETR and in further wide parameter ranges.

By analyzing the susceptibility terms of the PI growth rate, the pressure is found to be an important parameter determining the PI decay channels. In the low-pressure regime, ISQM is the dominant decay channel. It decreases rapidly with pressure and is eventually overtaken by the ICQM and its harmonics in the intermediate regime. In the high-pressure regime, only NILD decay channel is found.

Explicit forms of PI parameter dependence in each pressure regime are obtained by further analysis, which has been summarized in Table 1. The parameter dependence found in the low-pressure regime shows a good agreement with the published work.[21,22] In the intermediate regime, ICQMs display a quite different dependence from that in the low pressure due to the cyclotron motion of ions. For example, they may stop from increasing with n_e and even decrease if the density is low enough. In the high-pressure regime, where the perpendicular ion orbit is almost a straight line just like the parallel motion, the parameter dependence recovers to the same as ISQM.

PIs in CFETR are investigated by applying the above analytical results to a typical set of parameters of the hybrid scenario. Numerical calculations are also performed to verify and replenish the analytical conclusions. Along such an n_e-T_e coupled profile, all the three pressure regimes are found successively. The ISQM-dominant low-pressure regime occupies the outer half of SOL, while the inner half of SOL and the separatrix belong to the intermediate regime. The high-pressure regime occupies the region several centimeters inside the separatrix. As a result, the fundamental ICQM in the intermediate regime is the most unstable PI decay channel of

the profile, with a maximum growth rate comparable to the maximum growth rates in conventional tokamaks. Increasing parameters like B_0 or ω_0 can help reduce the dominant ICQM-type PI and the low growth rate of NILD, but has little effect on ISQM-type PI.

Through this work, the present understanding of PI parameter dependence is rearranged in the clue of pressure. For investigating PI in a certain position, we can now understand its decay channel and parameter dependence just by determining which pressure regime it locates. Sensitivities of parameter dependence are now clarified through the analytical expressions. For example, in the past, we only knew that the PI decays with an increasing T_e. Now we realize that for ICQM, the growth rate decays fastest with T_e in the intermediate regime and slowest in the low-pressure regime. This work also shows some situations with unforeseen parameter dependence. For instance, if the density of the intermediate regime is sufficiently low, the ICQM growth rate may stop from increasing with n_e and even decrease.

It should be noticed that the additional effects on sidebands such as plasma inhomogeneity and finite pump width may strongly limit the growth of sideband with high N_{1z} or a δ_1 near $\pi/2$, where δ_1 is the angle between $k_{0\perp}$ and $k_{1\perp}$.[37,38] These effects are not considered here because this paper mainly focuses on the analysis of the PI growth rate. Since a rather traditional version of PI model is used for the simplicity of the analysis, effects mentioned in the recent PI models such as collision and electromagnetic pumps could not be included.[39,40] The former can inhibit PIs near the antenna mouth, while the latter reduces PIs at high densities. In the future, more efforts on these issues will be made to refine the present results.

Appendix A: Derivation to an explicit form of the PI growth rate

When the PI occurs, both the child waves are influenced by a nonlinear PI growth rate $\gamma^{\rm NL}$. The LH sideband is usually a resonant mode here except the sidebands with rather high k_{1z}. Its frequency can be noted as $\omega_1 = \omega_{1r} + i\gamma^{\rm NL}$, where the subscript r represents the real part of the frequency. For the low-frequency mode, the frequency can be written as $\omega = \omega_r + i\gamma^{\rm NL} + i\gamma^{\rm L}$, where its linear damping rate $\gamma^{\rm L}$ is retained as it is a strongly damped quasi-mode in this paper.

In the theory of weak turbulence, the PI growth rate satisfies $\gamma^{\rm NL} \ll \omega_r, \omega_{1r}$. Using this relation, the linear dispersion relation of the sideband is expanded as $\varepsilon_1 \simeq i\gamma^{\rm NL}\frac{\partial \varepsilon_{1r}}{\partial \omega_{1r}}$. Substituting the expression into Eq. (1), we obtain

$$\gamma^{\rm NL} = {\rm Im}\left(\frac{\mu_1}{\varepsilon}\right) \Big/ \frac{\partial \varepsilon_{1r}}{\partial \omega_{1r}}. \tag{A1}$$

To give an explicit form of $\gamma^{\rm NL}$, the coefficients of μ_1, shown as Eqs. (7)–(9), are simplified to

$$\alpha_1 = \frac{e}{m_e}\frac{\phi_0}{2\omega_0}\chi_e\left[-\frac{ik_{0\perp}k_{1\perp}\sin\delta_1}{\omega_{ce}} - \frac{k_{0z}k_{1z}}{\omega_0}\right], \tag{A2}$$

$$\alpha_3 = \frac{e}{m_e}\frac{k^2}{k_1^2}\frac{\phi_0^*}{2\omega_0}\chi_e\left[-\frac{ik_{0\perp}k_{1\perp}\sin\delta_1}{\omega_{ce}} + \frac{k_{0z}k_{1z}}{\omega_0}\right], \tag{A3}$$

$$\beta_3 = \frac{k^2}{k_1^2}\frac{e}{m_e}\frac{\phi_0^*}{2\omega_{1r}}\left[-\frac{ik_{0\perp}k_{1\perp}\sin\delta_1}{\omega_{ce}} + \frac{k_{0z}k_{1z}}{\omega_0}\right]\alpha_1. \tag{A4}$$

Here, the electric field $\boldsymbol{E}_0$ is replaced by the electric potential ϕ_0 using $\boldsymbol{E}_0 = -i\boldsymbol{k}_0\phi_0$; δ_1 is the angle between the vector $\boldsymbol{k}_{1\perp}$ and $\boldsymbol{k}_{0\perp}$. The sideband frequency $\omega_{1r} = \omega_r - \omega_0$ is directly approximated as $-\omega_0$ since $\omega \ll \omega_0, \omega_1$. The matching conditions for the wave numbers are also used, so that $\omega k_{0z} - \omega_0 k_z = \omega_1 k_{0z} - \omega_0 k_{1z} \approx -\omega_0 k_z$ and $\boldsymbol{k}_\perp \times \boldsymbol{k}_{0\perp} = \boldsymbol{k}_{1\perp} \times \boldsymbol{k}_{0\perp}$.

Observing Eq. (A4), β_3 now can be directly written as $-\alpha_1\alpha_3/\chi_e$. The term μ_1/ε then becomes $\frac{\chi_e - \varepsilon}{\chi_e \varepsilon}\alpha_1\alpha_3$ and the PI growth rate is expanded as

$$\gamma^{\rm NL} = -\frac{e^2}{m_e^2}{\rm Im}\left[\frac{\chi_e(\chi_e - \varepsilon)}{\varepsilon}\right]\frac{\omega_0}{8\omega_{pe}^2}\frac{k^2}{k_{1z}^2} \times \left[\frac{k_{0\perp}^2 k_{1\perp}^2 \sin^2\delta_1}{\omega_{ce}^2} + \frac{k_{0z}^2 k_{1z}^2}{\omega_0^2}\right]\phi_0^2. \tag{A5}$$

To make the parameter dependence of $\gamma^{\rm NL}$ more clear, we transform the pump potential ϕ_0 into a realistic parameter such as the pump power P_0. The relation between them is approximately

$$P_0 = \frac{1}{4}\varepsilon_0 S\omega_0\frac{\omega_{pe}^2}{\omega_0^2}\frac{2k_{0\perp}^3 k_{0z}^2}{k_0^4}\phi_0^2. \tag{A6}$$

Using this relation, the PI growth rate then becomes

$$\gamma^{\rm NL} = \frac{e^2}{m_e^2}\frac{P_0}{2\varepsilon_0 S v_{te}^2}{\rm Im}\left(\frac{\kappa_i\kappa_e}{\kappa_i + \kappa_e}\right)\frac{\omega_0^2}{\omega_{pe}^2}\frac{k_0^4}{k_{0\perp}^3} \times \left[\frac{k_{0\perp}^2 k_{1\perp}^2 \sin^2\delta_1}{k_{0z}^2 k_{1z}^2 \omega_{ce}^2} + \frac{1}{\omega_0^2}\right]. \tag{A7}$$

The terms χ_e and ε are replaced by $\kappa_j = \frac{k^2 v_{tj}^2}{2\omega_{pe}^2}\chi_j$ for the j-th species, where the cold plasma condition $v_{te} \ll \omega_{pe}/k$ is also used.

For clarity, all the wave number terms in the above expression should be written as functions with respect to more realistic parameters. Using the linear dispersion relation of LHWs for edge plasmas $\omega_{pe} \ll \omega_{ce}$, we approximately write $\frac{k_{0\perp}^2}{k_{0z}^2} \approx \frac{k_{1\perp}^2}{k_{1z}^2} \approx \frac{\omega_{pe}^2}{\omega_0^2}$ and $k_{0\perp} \gg k_{0z}$. The left k_{0z} is represented by the refractive index $N_{0z} = k_{0z}c/\omega_0$, where c is the light speed in vacuum. The PI growth rate becomes

$$\gamma^{\rm NL} = \frac{e^2}{m_e^2}\frac{P_0 N_{0z}}{2\varepsilon_0 S c v_{te}^2}{\rm Im}\left(\frac{\kappa_i\kappa_e}{\kappa_i + \kappa_e}\right)\left(\frac{\omega_{pe}^3}{\omega_0^2\omega_{ce}^2} + \frac{1}{\omega_{pe}}\right), \tag{A8}$$

where the angle δ_1 has been set as $\pi/2$ to seek the maximum growth rate.

Acknowledgements

Project supported by the National Key Research and Development Program of China (Grant Nos. 2017YFE0300406 and 2019YFE00308050) and the National Natural Science Foundation of China (Grant Nos. 11975272, 12175274, 12005258, and 11705236). We sincerely appreciate the data support from the CFETR physics team.

References

[1] Luce T C 2011 *Phys. Plasmas* **18** 030501
[2] Giruzzi G, Artaud J F, Baruzzo M, Bolzonella T, Fable E, Garzotti L, Ivanova-Stanik I, Kemp R, King D B, Schneider M, Stankiewicz R, Stepniewski W, Vincenzi P, Ward D and Zagorski R 2015 *Nucl. Fusion* **55** 073002
[3] Fisch N J 1987 *Rev. Mod. Phys.* **59** 175
[4] Bernabei S, Daughney C, Efthimion P, Hooke W, Hosea J, Jobes F, Martin A, Mazzucato E, Meservey E, Motley R, Stevens J, Von Goeler S and Wilson R 1982 *Phys. Rev. Lett.* **49** 1255
[5] Song Y T, Wu S T, Li J G, Wan B N, Wan Y X, Fu P, Ye M Y, Zheng J X, Lu K, Gao X G, Liu S M, Liu X F, Lei M Z, Peng X B and Chen Y 2014 *IEEE Trans. Plasma Sci.* **42** 503
[6] Zhuang G, Li G Q, Li J, Wan Y X, Liu Y, Wang X L, Song Y T, Chan V, Yang Q W, Wan B N, Duan X R, Fu P, Xiao B J and the CFETR Design Team 2019 *Nucl. Fusion* **59** 112010
[7] Liu C S, Tripathi V K and Chan V S 1984 *Phys. Fluids* **27** 1709
[8] Takase Y, Porkolab M, Schuss J J, Watterson R L and Fiore C L 1985 *Phys. Fluids* **28** 983
[9] Cesario R, Amicucci L, Calabrò G, Cardinali A, Castaldo C, Marinucci M, Panaccione L, Pericoli-Ridolfini V, Tuccillo A A and Tudisco O 2009 *AIP Conf. Proc.* **1187** 419
[10] Liu C S and Tripathi V K 1986 *Phys. Rep.* **130** 143
[11] Cesario R and Cardinali A 1989 *Nucl. Fusion* **29** 1709
[12] Takase Y and Porkolab M 1983 *Phys. Fluids* **26** 2992
[13] Kindel J M, Okuda H and Dawson J M 1972 *Phys. Rev. Lett.* **29** 995
[14] Kaw P K, Lin A T and Dawson J M 1973 *Phys. Fluids* **16** 1967
[15] Porkolab M 1977 *Phys. Fluids* **20** 2058
[16] Porkolab M 1974 *Phys. Fluids* **17** 1432
[17] Tripathi V K 1977 *Phys. Fluids* **20** 1525
[18] Porkolab M, Bernabei S, Hooke W M, Motley R W and Nagashima T 1977 *Phys. Rev. Lett.* **38** 230
[19] Porkolab M, Schuss J J, Lloyd B, Takase Y, Texter S, Bonoli P, Fiore C, Gandy R, Gwinn D, Lipschultz E, Marmar E, Pappas D, Parker R and Pribyl P 1984 *Phys. Rev. Lett.* **53** 450
[20] Cesario R, Cardianli A, Castaldo C, Paoletti F and Mazon D 2004 *Phys. Rev. lett.* **92** 175002
[21] Napoli F, Castaldo C, Cesario R and Schettini G 2012 *J. Phys.: Conf. Ser.* **260** 12008
[22] Zhao A H and Gao Z 2013 *Nucl. Fusion* **53** 083015
[23] Cesario R, Amicucci L, Castaldo C, Marinucci M, Napoli F, Paoletti F, De Arcangelis D, Ferrari M, Galli A, Gallo G, Pullara E, Schettini G and Tuccillo A A 2014 *Nucl. Fusion* **54** 043002
[24] Ding B J, Li Y C, Zhang L, Li M H, Wei W, Kong E H, Wang M, Xu H D, Wang S L, Xu G S, Zhao L M, Hu H C, Jia H, Cheng M, Yang Y, Liu L, Zhao H L, Peysson Y, Decker J, Goniche M, Amicucci L, Cesario R, Tuccillo A A, Baek S G, Parker R, Bonoli P T, Paoletti F, Yang C, Shan J F, Liu F K, Zhao Y P, Gong X Z, Hu L Q, Gao X, Wan B N, Li J G and the EAST team 2015 *Nucl. Fusion* **55** 093030
[25] Baek S G, Parker R R, Bonoli P T, Shiraiwa S, Wallace G M, LaBombard B, Faust I C, Porkolab M and Whyte D G 2015 *Nucl. Fusion* **55** 043009
[26] Baek S G, Wallace G M, Bonoli P T, Brunner D, Faust I C, Hubbard A E, Hughes J W, LaBombard B, Parker R R, Porkolab M, Shiraiwa S and Wukitch S 2018 *Phys. Rev. Lett.* **121** 055001
[27] Cardinali A, Castaldo C, Cesario R, Santini F, Amicucci L, Ceccuzzi S, Galli A, Mirizzi F, Napoli F, Panaccione L, Schettini G and Tuccillo A A 2017 *Plasma Phys. Control. Fusion* **59** 074002
[28] Chen J L, Jia G Z and Xiang N 2021 *J. Fusion Energy* **40** 1
[29] Cesario R, Cardinali A, Castaldo C, Paoletti F, Fundamenski W, Hacquin S and the JET-EFDA workprogramme contributors 2006 *Nucl. Fusion* **46** 462
[30] Li M H, Ding B J, Zhang J Z, Gan K F, Wang H Q, Peysson Y, Decker J, Zhang L, Wei W, Li Y C, Wu Z G, Ma W D, Jia H, Chen M, Yang Y, Feng J Q, Wang M, Xu H D, Shan J F, Liu F K and EAST Team 2014 *Phys. Plasmas* **21** 062510
[31] Liu Z Y, Gao Z and Zhao A H 2019 *Phys. Plamsas* **26** 042117
[32] Triphathi V K, Liu C S and Grebogi C 1979 *Phys. Fluids* **22** 301
[33] Swanson D G 2003 *Plamsa Waves*, 2nd edn. (Auburn: Auburn University) p. 84
[34] Brambilla M 1976 *Plasma Phys.* **18** 669
[35] Glagolev V M 1972 *Plasma Phys.* **14** 301
[36] Liu L, Kessel C, Chan V, Guo Y, Chen J L, Jian X, Mao S F, Ye M Y and CFETR Physics Team 2018 *Nucl. Fusion* **58** 096009
[37] Rosenbluth M N 1972 *Phys. Rev. Lett.* **29** 565
[38] Chen L and Berger R L 1977 *Nucl. Fusion* **17** 779
[39] Castaldo C, Di Siena A, Fedele R, Napoli F, Amicucci L, Cesario R and Schettini G 2019 *Nucl. Fusion* **25** 016003
[40] Liu Z Y, Gao Z and Zhao A H 2020 *Phys. Plasmas* **27** 042503